This article has been accepted for inclusion in a future issue of this journal. Content is final as presented, with the exception of pagination.

Static Compliance Analysis and Control for Tendon-Pneumatic Hybrid-Driven Soft Actuators

Zhanxuan Peng, Yu Rong, Zhenpu Zhu, Jieji Ren, and Guoying Gu, *Senior Member, IEEE*

***Abstract*—Bellows-shaped soft actuators offer high dexterity, yet achieving both large workspace and high stiffness remains challenging. Tendon-pneumatic antagonistic actuation addresses this by expanding the workspace volume by 108.6% versus pure tendon-driven (TD) modes while retaining stiffness tunability. However, coupled actuation and complex geometry hinder accurate modeling. This article presents an ANCF-based compliance modeling and control framework for such actuators. First, the actuator is mapped to an equivalent cylindrical continuum with experimentally identified strain-dependent stiffness. Subsequently, closed-form compliance expressions are derived under constant-tension and fixed-length constraints, where an active-set procedure handles tendon slackness. A load-aware compliance controller (LACC) exploits the IK-derived compliance matrix as a built-in load observer for simultaneous position regulation and implicit load estimation. Simulations achieve positioning error below 0.03 mm within five iterations, reducing error by over 99% versus a virtual-force-based baseline. Experiments validate average shape-estimation errors below 2.5% and compliance-prediction errors below 5.0%.**

***Index Terms*—Absolute nodal coordinate formulation (ANCF), compliance modeling and control, kinetostatic model, soft continuum robot.**

I. Introduction

BELLOWS-SHAPED soft actuators exhibit superior extensibility and bending capability [1]. Owing to their highly deformable structures, their compliance varies considerably across different configurations. In many practical applications, it is desirable to simultaneously achieve accurate position control and tunable compliance, so that the actuator can deliver high stiffness for load-bearing tasks while preserving sufficient compliance for safe and dexterous interaction. Nevertheless, such on-demand regulation remains fundamentally challenging, since the diverse stiffening mechanisms, nonlinear elastic behavior, and variable cross-sectional geometry of bellows-shaped soft actuators significantly hinder accurate shape and compliance modeling.

Various stiffness-regulation mechanisms have been investigated in soft robotics. Jamming-based approaches [2] enable rapid soft-to-rigid transitions but compromise intrinsic compliance and resist analytical characterization [3]. Antagonistic strategies, such as dual-chamber pneumatic actuators modulating stiffness via differential pressure [4], preserve passive compliance at the cost of redundant chambers for multi-DOF (Degree of Freedom) motion [1], increasing volume and reducing volumetric efficiency. To achieve compact design, tendon-pneumatic hybrid actuation has emerged [5]. The axially arranged tendons provide contraction while pneumatic bellows generate extension, enabling continuous stiffness regulation and high force output [6], [7]. In addition, the tendon-pneumatic actuation is explicitly modelable, facilitating analytical compliance characterization. However, the strong inter-mode coupling, nonuniform bellows geometry, and strain-dependent stiffness under large deformation pose significant challenges for accurate kinetostatic modeling.

Various modeling approaches have been explored for coupled mechanics and compliance characterization. Classical beam theories (Euler-Bernoulli, Timoshenko) approximate the actuator as a cantilever beam [8], [9], but are limited to linear elasticity and small strains. For large deformations and material nonlinearities, piecewise constant curvature (PCC) models [10], [11], [12] and Cosserat rod theory [13], [14] have been widely adopted, enabling compliance modeling via linearized geometric constraints or Lie group formulations [12], [15], [16], [17]. However, PCC models suffer from reduced accuracy under complex loading, whereas Cosserat rod models incur substantial computational cost that limits real-time applicability [6], [18]. The complex geometry of bellows-shaped actuators poses additional challenges. To address this, data-driven methods [19], including physics-informed neural networks [18] and the Koopman operator [20], have been proposed to alleviate analytical complexity, but remain limited in interpretability and generalizability for explicit compliance analysis.

Achieving computational efficiency, high modeling accuracy, and closed-form compliance characterization remains a key challenge in soft robotics. The absolute nodal coordinate formulation (ANCF) addresses this by capturing nonlinear elastic deformation with relatively few degrees of freedom [21], [22].

Received 28 April 2026; revised 17 June 2026; accepted 4 July 2026. *(Corresponding author: Guoying Gu.)*

The authors are with the State Key Laboratory of Mechanical System and Vibration, School of Mechanical Engineering, Shanghai Jiao Tong University, Shanghai 200240, China, and also with Shanghai Key Laboratory of Intelligent Robotics, Shanghai Jiao Tong University, Shanghai 200240, China (e-mail: steven2606@sjtu.edu.cn; rongyu@sjtu.edu.cn; zhuzhenpu@sjtu.edu.cn; jiejiren@sjtu.edu.cn; guguoying@sjtu.edu.cn).

Digital Object Identifier 10.1109/TIE.2026.3713568

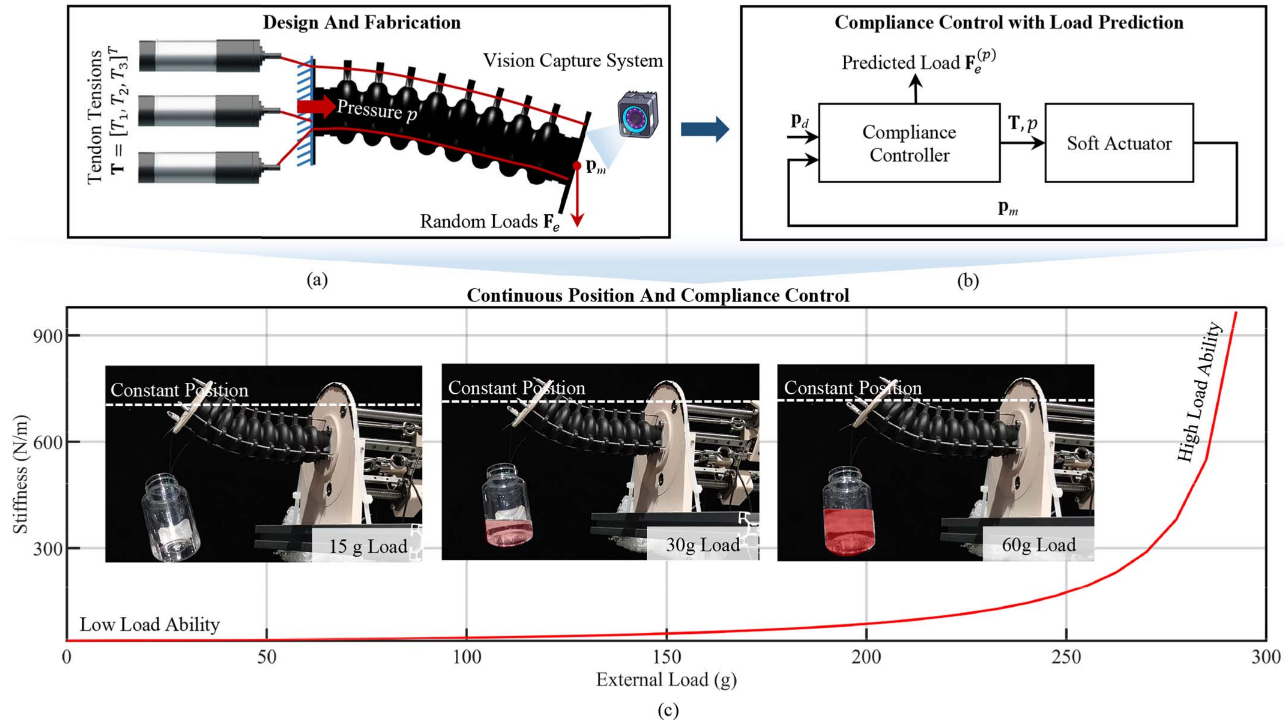

Fig. 1. Schematic illustration of the aim of this article. (a) Studying on the tendon-pneumatic hybrid-driven soft actuator. (b) We establish a novel compliance controller. (c) Which is applied for position and stiffness adjustment under stochastic loading. The red shaded area indicates water level.

Our prior work demonstrated the effectiveness of ANCF-based kinetostatic modeling for pneumatic soft actuators [1], [23], [24]. However, interaction-aware operation under unknown external loads requires not only position control but also explicit compliance regulation. The actuator must adjust its stiffness to accommodate external loads while maintaining task accuracy. Existing methods address this by solving load-estimation optimization problems [23], which incur prohibitive computational cost. Bridging this gap calls for an analytical compliance formulation within the ANCF framework that can be directly exploited for quasi-static interaction-aware control with low per-iteration cost.

As shown in Fig. 1, this article presents a kinetostatic modeling and load-aware compliance control (LACC) framework for tendon-pneumatic hybrid-driven bellows-shaped soft actuators. First, an ANCF-based model is developed to capture nonlinear elasticity and large-curvature deformation, enabling analytical compliance derivation under constant-tendon-tension and constant-tendon-length constraints. Subsequently, a LACC is designed for simultaneous position and stiffness regulation under stochastic loading. Simulations show 99% error reduction versus existing methods within five control steps. Experiments demonstrate 2.5% motion-control error and 5.0% compliance-estimation error, reducing the compliance-estimation error by 50% compared with the 10.0% error of prior Cosserat-based approaches [25].

The primary contributions of this work are as follows.

1) *Closed-form compliance expressions* are derived within the ANCF framework under constant-tension and fixed-length constraints, where an active-set procedure resolves the complementarity conditions from tendon slackness.
2) *A load-aware compliance controller (LACC)* that uses the IK-derived compliance matrix as a built-in load observer. Unlike Jacobian-transpose force observers assuming constant stiffness, LACC embeds the full configuration-dependent mechanical impedance, enabling simultaneous position regulation and implicit load estimation at the cost of a single IK iteration per step.

The remainder of this article is organized as follows. Section II introduces the actuator design and establishes the ANCF-based kinetostatic model. Section III derives the kinetostatic mappings from actuation inputs to tip configuration. Closed-form compliance expressions are then obtained under constant-tension and fixed-length constraints. The LACC is subsequently proposed. Section IV validates the framework through simulation studies. Section V presents experimental validation, covering shape estimation, stiffness prediction, and compliance control. Section VI concludes the article.

II. Kinetostatic Model

This section establishes the kinetostatic model for the tendon-pneumatic hybrid-driven soft actuator. First, the robot system description is provided, followed by the modeling assumptions and simplifications. The actuator deformation is then described using the ANCF framework, with the configuration parameterized by shape functions and global nodal positions and gradients. Finally, a kinetostatic model is derived to relate the hybrid actuation inputs to the equilibrium configuration.

A. Robot System Description

The mechanical system comprises a bellows-shaped soft actuator, a tendon-drive module, and a pneumatic module

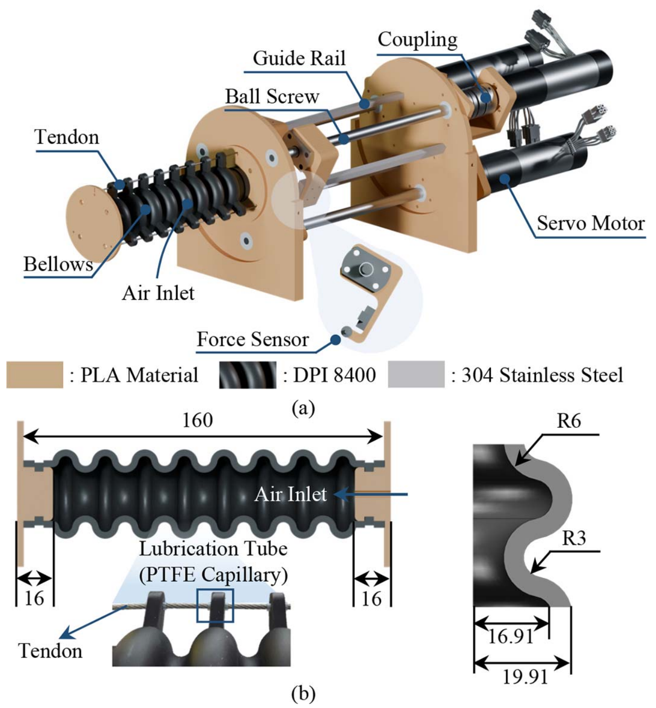

Fig. 2. Design and fabrication of the bellows-shaped soft actuator. (a) Mechanical structure. (b) Design parameters (unit: mm).

[Fig. 2(a)]. The bellows body is vacuum-cast in hyperelastic material DPI8400 silicone rubber (Shore 50 A). Two polylactic acid (PLA) end caps with tendon-routing holes are 3-D-printed, one incorporating an air inlet. After assembly, silicone adhesive ensures airtight sealing, and polytetrafluoroethylene (PTFE) capillaries line the tendon channels to reduce friction. Three 7×7 stainless-steel tendons (1.5-mm diameter) are threaded through the actuator, anchored distally, and coupled proximally to force sensors [Fig. 2(b)]. Driven by one pneumatic chamber and three peripheral tendons, the actuator achieves elongation, contraction, and bending. With four independent actuation inputs (three tendon tensions and one pneumatic pressure), the system can control the 3-DoF tip position while simultaneously regulating the compliance along any desired direction. The 160 mm length provides a representative length-to-diameter ratio ($\approx$ 5.4:1) for applications such as endoscopic procedures and confined-space inspection, while facilitating laboratory-scale validation.

B. Modeling Simplification

Following the methodology established in [1], the bellows-shaped soft actuator is modeled as an equivalent cylindrical continuum with a constant cross-sectional diameter D_a and an effective actuation diameter D_{eff}. This approximation has been thoroughly validated in [1], demonstrating configuration prediction errors of 3.43%. These equivalent parameters are identified experimentally by fitting the actuator deformation response, which yields $D_a = 29.59$ mm and $D_{\text{eff}} = 26.05$ mm. The detailed fitting procedure is reported in [1]. Over the operating range considered in this study, the actuator is represented by an experimentally identified effective structural stiffness $k(\lambda) = a\lambda + b = 1336\lambda - 568.8$, where λ is the axial strain ratio. Since the pneumatic chambers and tendons are arranged in parallel, torsional effects are neglected, and the deformation is assumed to be restricted to axial extension, contraction, and bending. Accordingly, the tensile and bending stiffnesses are expressed as $k_t = k(\lambda)l_0$ and $k_b = D_a^2 l_0 \lambda k(\lambda)/8$, respectively, where l_0 is the original length of the ANCF element. The detailed derivation follows [1] and is omitted here for brevity.

Two modeling simplifications and their treatment warrant explicit discussion. First, tendon friction along the PTFE-lined routing path is neglected in the kinetostatic model. Under large bending, lateral tendon-hole contact introduces Coulomb friction that slightly reduces the effective tension at the distal anchorage. Second, bellows self-contact is not explicitly modeled. Under upward bending with applied tip loads, adjacent convolutions may contact, producing unmodeled local stiffening. These two effects are the primary causes of the 3–6% stiffness prediction error observed in Section V.

C. Kinematics

Adopting the gradient deficient ANCF, the centerline is discretized into n elements (Fig. 3). For the i-th element with original length l_0, the states are parameterized by a reference arc length parameter $x \in [0, l_0]$. Its configuration is described by the position vector $\mathbf{r}$ and its spatial gradient $\mathbf{r}_x$, defining the nodal coordinates as $\mathbf{q}(x) = \left[\mathbf{r}^T, \mathbf{r}_x^T\right]^T \in \mathbb{R}^6$. The position field within the i-th element is interpolated using a shape function $\mathbf{S}(x) \in \mathbb{R}^{3\times 12}$ constructed from cubic Hermitian polynomials to ensure C^1 continuity $\mathbf{S}(x) = [s_1\mathbf{I}_3, \quad s_2\mathbf{I}_3, \quad s_3\mathbf{I}_3, \quad s_4\mathbf{I}_3] \in \mathbb{R}^{3\times 12}$, where $\mathbf{I}_3$ is the 3×3 identity matrix. The scalar shape functions s_i are explicitly given by the normalized coordinate $\xi = x/l_0 \in [0, 1]$: $s_1 = 1 - 3\xi^2 + 2\xi^3, s_2 = l_0(\xi - 2\xi^2 + \xi^3), s_3 = 3\xi^2 - 2\xi^3, s_4 = l_0(-\xi^2 + \xi^3)$. The position $\mathbf{r}_x$ is then calculated as $\mathbf{r}(x) = \mathbf{S}(x)\mathbf{q}^i$, where $\mathbf{q}^i = \left[\mathbf{q}_i^T, \mathbf{q}_{i+1}^T\right]^T$. Based on the above parameterized method and large deformation assumption, the Green strain tensor $\varepsilon(x)$ and the curvature $\kappa(x)$ along the i-th element are calculated as $\varepsilon(x) = (1/2)(\mathbf{r}_x^T\mathbf{r}_x - 1)$ and $\kappa(x) = (\|\mathbf{r}_x \times \mathbf{r}_{xx}\|/\|\mathbf{r}_x\|^3)$, respectively. The $(\cdot)_{xx}$ and $\|\cdot\|$ denote the second derivatives with respect to x and the l_2-norm of the vector, respectively. The deformation of the entire actuator can be described by concatenating the $n+1$ nodes as $\mathbf{q} = \left[\mathbf{q}_1^T, \mathbf{q}_2^T, \ldots, \mathbf{q}_i^T, \mathbf{q}_{i+1}^T, \ldots, \mathbf{q}_n^T, \mathbf{q}_{n+1}^T\right]^T$.

D. Kinetostatic Model

To determine the nodal coordinates $\mathbf{q}$, the kinetostatic equilibrium is established based on the principle of virtual work [1]. For the i-th element of the tendon-pneumatic hybrid-driven actuator, the generalized force balance is expressed as $\mathbf{Q}_t^i + \mathbf{Q}_b^i - \mathbf{Q}_g^i - \sum_{j=1}^{3}\mathbf{Q}_{cj}^i - \mathbf{Q}_p^i - \mathbf{Q}_f^i = \mathbf{0}$, where $\mathbf{Q}_t^i$, $\mathbf{Q}_b^i$, $\mathbf{Q}_g^i$, $\mathbf{Q}_{cj}^i$, $\mathbf{Q}_p^i$, and $\mathbf{Q}_f^i$ denote the generalized tensile force, generalized bending force, generalized gravity force, generalized tendon force, generalized pneumatic force, and generalized external force, respectively. The elastic-force terms are derived from a linear elastic constitutive model through the variation of the corresponding potential energies, whereas the load-induced terms

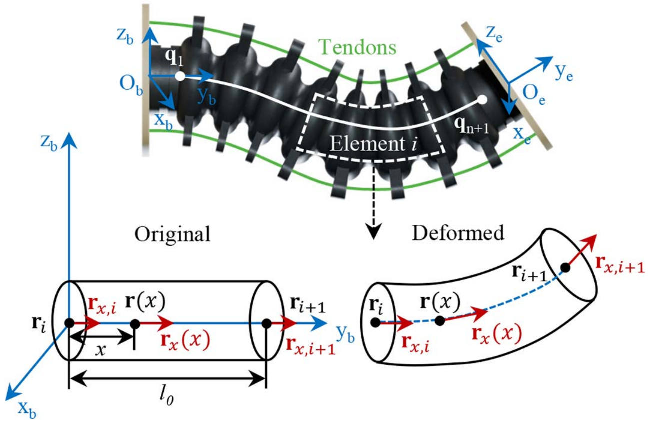

Fig. 3. Schematic of the actuator configuration and coordinate definitions. The nodal coordinates $\mathbf{q}_i$ are defined along the soft bellows section.

are derived using the principle of virtual work. Specifically, the virtual work W^i of each external action is first formulated and then expressed in terms of the generalized-coordinate variation $\delta\mathbf{q}^i$, from which the corresponding generalized force $\mathbf{Q}^i = (\partial W^i/\partial \mathbf{q}^i)^T \in \mathbb{R}^{12}$ is identified. The detailed expressions are provided in Supplementary Material Section S1. The nodal coordinate of the i-th element $\mathbf{q}^i$ and the nodal coordinate of the soft actuator $\mathbf{q}$ satisfy $\mathbf{q}^i = \mathbf{B}^i\mathbf{q}$, where $\mathbf{B}^i \in \mathbb{R}^{12\times 6(n+1)}$ is the Boolean matrix. Using the Boolean matrix, the kinetostatic model of the soft actuator with n elements can be expressed as

$$\mathbf{Q}_t + \mathbf{Q}_b - \mathbf{Q}_g - \sum_{j=1}^{3} \mathbf{Q}_{cj} - \mathbf{Q}_p - \mathbf{Q}_f = \mathbf{0} \in \mathbb{R}^{6n+6} \tag{1}$$

where each $\mathbf{Q}\star$ is assembled from its element-level counterparts $\mathbf{Q}\star^i$ via $\mathbf{Q}\star = \sum_{i=1}^{n} (\mathbf{B}^i)^T \mathbf{Q}\star^i$.

The proposed compliance model rests on the ANCF kinematics with the Green strain measure, the experimentally identified strain-dependent stiffness $k(\lambda)$ that captures hyperelastic material nonlinearity, and a local linearization of the equilibrium equations to obtain the analytical compliance matrix. The linearization accuracy is guaranteed near equilibrium and self-corrects as the iterative LACC loop drives the configuration toward the target. Across the tested operating range (0–120 kPa, 0–5 N tendon tension), shape-estimation errors remain below 2.5% (Section V-B) and stiffness-prediction errors are 3–6% (Section V-C). Compared with PCC-based formulations that degrade under complex loading and Cosserat-rod approaches that incur high computational cost from iterative integration, the ANCF framework uniquely provides analytical closed-form compliance expressions while capturing nonlinear large-deformation effects with relatively few degrees of freedom.

III. Kinetostatic Mappings and Load-Aware Compliance Control Strategy

This section first establishes the forward and inverse kinetostatic (IK) mappings. In addition, the deformation under constant tendon-length constraints is analyzed. Analytical compliance expressions are then established under both constant tendon-force and constant tendon-length constraints. Finally, a LACC strategy is proposed to adaptively regulate the soft actuator under uncertain loading conditions.

A. Kinetostatic Mapping for Tendon-Force Actuation

The forward kinetostatic (FK) problem aims to determine the nodal coordinates $\mathbf{q}$ of the soft actuator for a given set of actuation inputs. Let $\boldsymbol{\tau} = [\mathbf{T}^T, p]^T = [T_1, T_2, T_3, p]^T$ denote the actuation vector, where T_i represents the tension of the i-th tendon and p is the internal pneumatic pressure. Formally, the FK mapping $\mathcal{F} : (\mathbf{T}, p, \mathbf{F}_e) \to \mathbf{q}$ is defined by the following equilibrium condition $\mathbf{Q}(\mathbf{q}, \mathbf{T}, p, \mathbf{F}_e) = \mathbf{0}$, where $\mathbf{Q}(\mathbf{q}, \mathbf{T}, p, \mathbf{F}_e)$ refers to (1). The equations can be numerically solved by the Levenberg-Marquardt (L-M) algorithm given the initial guess of all unknown variables.

The IK problem is formulated as identifying the required tensions $\mathbf{T}$ and the corresponding nodal coordinates $\mathbf{q}$ to achieve a target tip position $\mathbf{p}_{\text{end}}$. Given a desired tip position $\mathbf{p}_d \in \mathbb{R}^3$ and a pneumatic pressure p, the IK mapping $\mathcal{F}^{-1} : (\mathbf{p}_d, p) \to (\mathbf{q}, \mathbf{T})$ seeks to determine $(\mathbf{q}, \mathbf{T})$ such that

$$\begin{aligned} &\text{find} \quad (\mathbf{q}, \mathbf{T}) \\ &\text{s.t.} \ \mathbf{Q}(\mathbf{q}, \mathbf{T}, p, \mathbf{F}_e) = \mathbf{0} && \text{(2a)} \\ &\quad\ \ \mathbf{p}_{\text{end}}(\mathbf{q}_{n+1}) - \mathbf{p}_d = \mathbf{0}. && \text{(2b)} \end{aligned}$$

The global tip position, denoted as $\mathbf{p}_{\text{end}}$, differs from the position of the last node $\mathbf{r}_{n+1}$ due to the rigid tool offset along the axial direction. By utilizing the last nodal coordinates $\mathbf{q}_{n+1}$, the orientation of the tip is analytically determined via Rodrigues' rotation formula.

B. Kinetostatic Mapping for Tendon-Length Actuation

In tendon-driven (TD) actuators, the desired configuration is typically obtained from $\mathcal{F}^{-1}$, after which the motors are held at zero velocity. The actuator becomes tendon-length constrained. Under an external tip load $\mathbf{F}_e$, tendons along contracting paths will become slack and carry zero tension. Let β_i denote the slackness of the i-th tendon. Then, T_i and β_i satisfy the following complementarity conditions:

$$\tau_i \geq 0, \quad \beta_i \geq 0, \quad \tau_i\beta_i = 0, \quad i \in \{1, 2, 3\}. \tag{3}$$

Accordingly, the equilibrium equation, which couples the generalized force balance and the length-slackness constraints, is expressed as

$$\begin{cases} \mathbf{Q}(\mathbf{q}, \mathbf{T}, p, \mathbf{F}_e) = \mathbf{0} \\ l_{c,i}(\mathbf{q}) + \beta_i - l_{c,i}^0 = 0, \quad i \in \{1, 2, 3\} \end{cases} \tag{4}$$

where $l_{c,i}^0$ denotes the fixed tendon length at the moment the motors were locked. The specific expression of the i-th tendon length in the j-th element $l_c(\mathbf{q}^j, d_i, \theta_i)$ is described in Supplementary Material. The i-th tendon length $l_{c,i}(\mathbf{q})$ can be calculated by summing the tendon length for all ANCF elements

$$l_{c,i}(\mathbf{q}) = \sum_j l_c(\mathbf{q}^j, d_i, \theta_i). \tag{5}$$

By combining (3) and (4), the equilibrium configuration under constant tendon-length constraints can be determined. To handle the resulting complementarity conditions, we adopt the auxiliary-variable formulation in [16], [26]. Specifically, an auxiliary variable γ_i, $i \in \{1,2,3\}$, is introduced to unify the tendon tension T_i and slackness β_i as

$$T_i = \begin{cases} \gamma_i^2, & \text{if } \gamma_i > 0 \\ 0, & \text{if } \gamma_i \leq 0 \end{cases}, \beta_i = \begin{cases} 0, & \text{if } \gamma_i > 0 \\ \gamma_i^2, & \text{if } \gamma_i \leq 0. \end{cases} \tag{6}$$

This substitution regularizes the unilateral constraints and converts (4) into a system of algebraic equality equations for numerical solution. The FK and IK mappings can be formulated in a manner similar to $\mathcal{F}$ and $\mathcal{F}^{-1}$, respectively.

C. Static Compliance Analysis for Tendon-Force Actuation

To characterize the structural compliance under tendon-force actuation, the analytical compliance is derived. It defines the sensitivity of the tip position to external tip loads. Given the equilibrium equation $\mathbf{Q}(\mathbf{q}, \mathbf{T}, p, \mathbf{F}_e) = \mathbf{0}$ in (1), the configuration-space compliance is obtained under constant tendon force ($\delta\mathbf{T} = \mathbf{0}$) and constant pressure ($\delta p = 0$) as

$$\delta\mathbf{Q} = \frac{\partial\mathbf{Q}}{\partial\mathbf{q}}\delta\mathbf{q} + \frac{\partial\mathbf{Q}}{\partial\mathbf{T}}\delta\mathbf{T} + \frac{\partial\mathbf{Q}}{\partial p}\delta p + \frac{\partial\mathbf{Q}}{\partial\mathbf{F}_e}\delta\mathbf{F}_e = \mathbf{0} \tag{7}$$

$$\delta\mathbf{q} = -\left(\frac{\partial\mathbf{Q}}{\partial\mathbf{q}}\right)^{-1}\left(\frac{\partial\mathbf{Q}}{\partial\mathbf{F}_e}\right)\delta\mathbf{F}_e = \mathbf{C_q}\delta\mathbf{F}_e \tag{8}$$

where $\mathbf{C_q} \in \mathbb{R}^{(6n+6)\times 3}$ denotes the sensitivity of the nodal coordinates $\mathbf{q}$ to the external load perturbation $\delta\mathbf{F}_e$. The task-space compliance is then given by

$$\delta\mathbf{p}_{\text{end}} = \left(\frac{\partial\mathbf{p}_{\text{end}}}{\partial\mathbf{q}_{n+1}}\right)\delta\mathbf{q}_{n+1} \tag{9}$$

$$\mathbf{C_p} = \left(\frac{\partial\mathbf{p}_{\text{end}}}{\partial\mathbf{q}_{n+1}}\right)\mathbf{C}_{\mathbf{q}}^{\text{sub}} \tag{10}$$

where $\mathbf{C}_{\mathbf{q}}^{\text{sub}} \in \mathbb{R}^{6\times 3}$ is the sub-matrix of $\mathbf{C_q}$ associated with the last-node coordinates $\mathbf{q}_{n+1}$.

D. Static Compliance Analysis for Tendon-Length Actuation

Under constant tendon-length actuation, the tendon lengths $l_{c,i}$ are fixed at their motor-locking values $l_{c,i}^0$. Direct compliance analysis based on (4) is analytically complex and computationally costly. A simplified method is proposed for the locked configuration.

In the locked state, stiffness is dominated by geometric constraints from taut tendons. Under a perturbation $\delta\mathbf{F}_e$, some tendons remain taut while others slacken. The $\mathbf{C_q}$ in (10) is derived under a local linearization assumption. It captures the instantaneous response direction of the configuration change. Simulations indicate that the linearization remains accurate for tip loads up to approximately 200 g. Beyond this range, the compliance-based load estimate degrades and the controller defaults to a pure IK-based position correction (Section III-E). The initial nodal displacement is estimated as $\delta\mathbf{q}_{\text{est}} \approx \mathbf{C_q}\delta\mathbf{F}_e$. The corresponding variation in the i-th tendon length is approximated by $\delta l_{c,i} \approx (\partial l_{c,i}/\partial\mathbf{q})\delta\mathbf{q}_{\text{est}}$, where the expression of $\partial l_{c,i}/\partial\mathbf{q}$ is provided in the Supplementary Material. A tendon is included in the active constraint set $\mathcal{A}$ if $\delta l_{c,i} > 0$, indicating that it remains taut under actuator lock. Otherwise, if $\delta l_{c,i} \leq 0$, the tendon is considered to be slackening and removed from the rigid-length constraints in the subsequent analysis.

Once the active set $\mathcal{A}$ is identified, the system is constrained by both force equilibrium and the rigid constraints of taut tendons. Under the assumption of small perturbations, tendon tensions are approximated by their prelocking equilibrium values $\mathbf{T}_0 = [T_1^0, T_2^0, T_3^0]^T$. With the pneumatic pressure maintained at p_0, the augmented equilibrium equations near the locking configuration are formulated as

$$\begin{cases} \mathbf{Q}(\mathbf{q}, \mathbf{T}_0, p_0, \mathbf{F}_e) = \mathbf{0} \\ l_{c,i}(\mathbf{q}) - l_{c,i}^0 = 0, \quad i \in \mathcal{A}. \end{cases} \tag{11}$$

The task-space compliance is then derived by differentiating (11)

$$\begin{bmatrix} \frac{\partial\mathbf{Q}}{\partial\mathbf{q}} & -\mathbf{J}_{\mathcal{A}}^T \\ \mathbf{J}_{\mathcal{A}} & \mathbf{0}_{n(\mathcal{A})\times n(\mathcal{A})} \end{bmatrix} \begin{bmatrix} \delta\mathbf{q} \\ \delta\mathbf{T}_{\mathcal{A}} \end{bmatrix} = \begin{bmatrix} -\frac{\partial\mathbf{Q}}{\partial\mathbf{F}_e} \\ \mathbf{0}_{n(\mathcal{A})\times 3} \end{bmatrix} \delta\mathbf{F}_e \tag{12}$$

where $J_{\mathcal{A}} = (\partial\mathbf{l}_{\mathcal{A}}/\partial\mathbf{q}) \in \mathbb{R}^{n(\mathcal{A})\times(6n+6)}$ is the Jacobian of the active tendon-length constraints, and $n(\mathcal{A})$ denotes the number of active tendon-length constraints. The term $\delta\mathbf{T}_{\mathcal{A}}$ represents the variation in active tensions, which is assumed to be negligible ($\delta\mathbf{T}_{\mathcal{A}} \approx \mathbf{0}$). To account for tendon-length constraints, the configuration-space compliance is derived as

$$\delta\mathbf{q} = \mathbf{C}'_{\mathbf{q}}\delta\mathbf{F}_e = -\begin{bmatrix} \frac{\partial\mathbf{Q}}{\partial\mathbf{q}} \\ \mathbf{J}_{\mathcal{A}} \end{bmatrix}^{-1} \begin{bmatrix} \frac{\partial\mathbf{Q}}{\partial\mathbf{F}_e} \\ \mathbf{0}_{n(\mathcal{A})\times 3} \end{bmatrix} \delta\mathbf{F}_e. \tag{13}$$

The pseudoinverse in (13) is computed via singular value decomposition (SVD). Furthermore, the task-space configuration $\mathbf{C}'_{\mathbf{p}}$ is derived analogously to (10).

It is worth noting that the system's compliance can also be formulated through the inverse kinematics mapping, where the augment equilibrium equations are

$$\begin{cases} \mathbf{Q}(\mathbf{q}, \mathbf{T}_0, p, \mathbf{F}_e) = \mathbf{0} \\ \mathbf{p}_{\text{end}} - \mathbf{p}_d = \mathbf{0} \\ l_{c,i}(\mathbf{q}) - l_{c,i}^0 = 0, \quad i \in \mathcal{A}. \end{cases} \tag{14}$$

The $\mathbf{p}_d$ is the tip position of the prelocking state. Specifically, the state variation $\delta\mathbf{q}$ is obtained by differentiating (14)

$$\delta\mathbf{q} = \mathbf{C}'_{\mathbf{q}}\delta\mathbf{F}_e = -\mathbf{H}_{IK}^{-1}\begin{bmatrix} \frac{\partial\mathbf{Q}}{\partial\mathbf{F}_e} \\ \mathbf{0}_{(n(\mathcal{A})+3)\times 3} \end{bmatrix}\delta\mathbf{F}_e \tag{15}$$

where $\mathbf{H}_{IK} = \left[(\partial\mathbf{Q}/(\partial\mathbf{q}))^T, (\partial\mathbf{p}_{\text{end}}/(\partial\mathbf{q}))^T, \mathbf{J}_{\mathcal{A}}^T\right]^T$ represents the Jacobian of the constrained equations. Here, the end-effector Jacobian is partitioned as $(\partial\mathbf{p}_{\text{end}}/\partial\mathbf{q}) = [\mathbf{0}_{3\times 6n}, (\partial\mathbf{p}_{\text{end}}/\partial\mathbf{q}_{n+1})]$. According to the nodal discretization. The resulting task-space compliance $\mathbf{C}'_{\mathbf{p}}$ is shown as follows:

$$\mathbf{C}'_{\mathbf{p}} = \left(\frac{\partial\mathbf{p}_{\text{end}}}{\partial\mathbf{q}_{n+1}}\right)(\mathbf{C}'_{\mathbf{q}})^{\text{sub}} \tag{16}$$

where $(\mathbf{C}'_{\mathbf{q}})^{\text{sub}}$ denotes the subset of the configuration-space compliance matrix corresponding to the tip node. Numerical evaluations reveal that the compliance formulation in (16) provides a more accurate gradient for the load estimation loop, leading to faster convergence compared with the FK-based counterpart. Consequently, this IK-based compliance is utilized in all subsequent control implementations.

It is worth noting that although the constant-tendon-length compliance derivation in this section formally treats tendon length as the primary constraint variable, the pneumatic pressure p_0 is explicitly retained in the equilibrium equations (11) and directly influences compliance through two mechanisms. First, a higher pressure increases the axial strain λ, which raises the strain-dependent stiffness $k(\lambda)$ and thus stiffens the actuator. Second, the pressure shifts the prelocking equilibrium configuration $(\mathbf{q}, \mathbf{T}_0)$, which in turn determines the active tendon set $\mathcal{A}$ and the Jacobian $\mathbf{J}_{\mathcal{A}}$ that govern the compliance matrix $\mathbf{C}'_{\mathbf{p}}$. The coupling between tendon-length constraints and pneumatic pressure is therefore intrinsically captured in the derived compliance expressions without requiring additional coupling terms.

E. Load-Aware Compliance Control Strategy

To demonstrate the effectiveness of the established compliance model, this section further presents a load-aware compliance control (LACC) strategy to regulate actuator's position and tip compliance simultaneously. The specific algorithm is shown in Algorithm 1. When the measured tip position $\mathbf{p}_m$ is away from the desired tip position $\mathbf{p}_d$ in motors' zero-velocity locking state, the discrepancy $\mathbf{e} = \mathbf{p}_d - \mathbf{p}_m$ is primarily attributed to the structural deformation governed by the system compliance. By inverting the compliance matrix $\mathbf{C}'_{\mathbf{p}}$, we can update the estimated external load with $\mathbf{F}_e^{(k+1)} = \mathbf{F}_e^{(k)} + \mathbf{C}'^{-1}_{\mathbf{p}}(\mathbf{p}_m - \mathbf{p}_d)$, where $\mathbf{F}_e^{(k)}$ denotes the estimated end load at the k-th control step. This formulation serves as a compliance-weighted integral law. Each control cycle involves only a single IK resolution and two compliance matrix evaluations. Since the compliance matrices are derived as intrinsic by-products of the IK solving process, the proposed algorithm imposes minimal computational burden per control step, making it practical for quasi-static interaction tasks. Since $\mathbf{C}'_{\mathbf{p}}$ is derived via local linearization, its accuracy is guaranteed for loads up to approximately 200 g. Beyond this range, the compliance-based load estimate degrades. The controller then defaults to pure IK-based position correction, which remains effective irrespective of load magnitude. Within the valid range, the iterative scheme is self-accelerating. Early iterations provide coarse corrections under large perturbations, and later iterations operate in a near-equilibrium regime where the linearized compliance is asymptotically exact.

Regarding the IK solver initialization, the first IK problem in each control episode uses the gravity-only droop configuration (calculate in advance and save) as the initial nodal-coordinate guess $\mathbf{q}_0$. All subsequent IK calls adopt the converged $\mathbf{q}$ from the previous IK solution as the initial guess. This warm-start strategy exploits the small configuration change between consecutive control steps and effectively prevents convergence to local optima or singular configurations. The Levenberg-Marquardt solver uses a damping factor of 0.01 and a convergence tolerance of 10^{-6} on the residual norm.

Algorithm 1: Load-Aware Compliance Controller.

Input: Desired position $\mathbf{p}_d$, initial load $\mathbf{F}_e^0$, pressure p.
Output: Tendon lengths $\mathbf{l}_c$, predicted external load $\mathbf{F}_e$.
Initialize $\mathbf{F}_e \leftarrow \mathbf{F}_e^0$.
$[\mathbf{q}, \mathbf{T}] \leftarrow$ Calculate (2) according to $\mathbf{F}_e^0, \mathbf{p}_d, p$.
while $\|\mathbf{p}_m - \mathbf{p}_d\| \geq 0.2$ mm **do**
  $\mathbf{p}_m \leftarrow$ Get current end position from visual system.
  $\mathbf{C}_{\mathbf{q}} \leftarrow$ Calculate (8) according to $\mathbf{q}, \mathbf{p}_d, \mathbf{T}, p$.
  $\mathcal{A} \leftarrow$ Get active constraint set with $\delta l_{c,i} \approx \frac{\partial l_{c,i}}{\partial \mathbf{q}} \delta \mathbf{q}_{est}$.
  $\mathbf{C}'_{\mathbf{p}} \leftarrow$ Calculate (15) according to $\mathcal{A}, \mathbf{q}, \mathbf{p}_d, \mathbf{T}, p$.
  $\mathbf{F}_e \leftarrow \mathbf{F}_e + \mathbf{C}'^{-1}_{\mathbf{p}}(\mathbf{p}_m - \mathbf{p}_d)$.
  $\mathbf{q}, \mathbf{T} \leftarrow$ Calculate (2) according to $\mathbf{F}_e, \mathbf{p}_d, p$.
  $\mathbf{l}_c \leftarrow$ Calculate (5) according to $\mathbf{q}$.
  Move to the calculated tendon lengths $\mathbf{l}_c$.
end while
return $\mathbf{l}_c, \mathbf{F}_e$

IV. Simulation Studies

This section evaluates the proposed framework through simulations. Workspace analysis is first conducted to assess the reachability gain of the hybrid actuation scheme. The proposed compliance controller is then benchmarked against an existing method in terms of positioning accuracy. The results support the subsequent experimental validation.

A. Workspace Analysis

To evaluate the reachability of the hybrid actuation scheme, the actuator workspace is analyzed in TD and tendon-pneumatic hybrid-driven (TPHD) modes. For each mode, 10 000 randomly sampled actuation inputs are obtained through Monte Carlo method. In the TD mode, $p = 0$ kPa and the tendon tensions are constrained to $[0, 5]$ N. In the TPHD mode, the same tension limits are used, while p varies within $[0, 120]$ kPa. The FK problem $\mathcal{F}$ is solved for each sample to obtain the tip position. The workspace volume is obtained by calculating the maximum convex hull volume for each actuation mode. As shown in Fig. 4, pneumatic pressurization offsets tendon-induced compression and enlarges the reachable bending range. Consequently, the TPHD mode increases the workspace volume by 108.6% compared with the TD mode.

B. Benchmarking of Compliance Control Performance

The proposed LACC is benchmarked against a virtual-force-based compliance controller (VF-CC) [25]. In VF-CC, the measured position error $\Delta\mathbf{p} = \mathbf{p}_m - \mathbf{p}_d$ is converted to a virtual tip force, and the IK problem is then solved with this virtual force incorporated as an additional load. Simulations are conducted in three representative configurations: upward, horizontal, and downward, with the VF-CC virtual-force proportional gains χ_x,

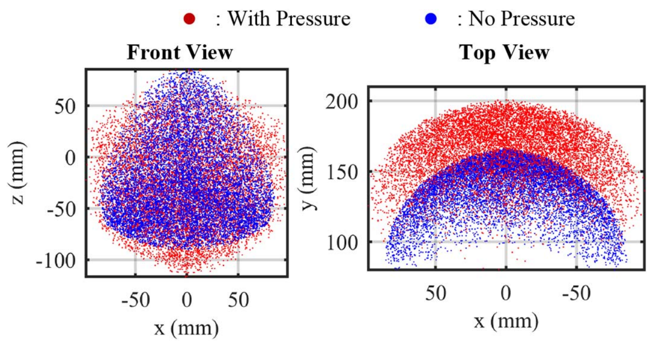

Fig. 4. Workspace comparison between the tendon-driven mode (blue) and the tendon-pneumatic hybrid-driven mode (red).

TABLE I
CONTROL ERROR AFTER FIVE ITERATIONS

Actuator Configuration	Error With VF-CC	Error With LACC	Error Reduction
Upward	9.054 mm	0.020 mm	99.78 %
Horizontal	10.23 mm	0.028 mm	99.73 %
Downward	2.090 mm	0.006 mm	99.71 %

TABLE II
COMPARISON OF OPEN-LOOP MOTION CONTROL

Reference	Method	Hyper-Elasticity	Position Error
[11]	PCC	No	3.22 mm (2.4%)
[14]	Cosserat	Yes	1.40 mm (3.1%)
[28]	Network	-	11.4 mm (2.7%)
[29]	ANCF	No	6.20 mm (3.5%)
Our Work	ANCF	Yes	3.43 mm (2.5%)

χ_y, χ_z set to 10. Fig. 5 shows that VF-CC, which lacks explicit load prediction, cannot distinguish load-induced deformation from actuation-induced motion. By contrast, LACC incorporates an iterative load observer to estimate the actuator state under external loading. As summarized in Table I, after five iterations, the residual errors of LACC are 0.020, 0.028, and 0.006 mm in the upward, horizontal, and downward configurations, respectively, compared with 9.054, 10.23, and 2.090 mm for VF-CC. Across all cases, LACC reduces the control error by more than 99.71% within the same iteration limit. An additional ablation study confirms that the IK-derived compliance matrix converges 50% faster than its FK-derived counterpart (Section III-D), validating the design choice of exploiting the IK solution. Additional results under multiaxis loads are provided in Supplementary Material Section S4. Model-based compliance control for soft continuum robots remains an under-explored area. The VF-CC [25] is the most directly comparable baseline with closed-loop compliance regulation, while other related works either address compliance analysis without control, regulate stiffness via external mechanisms, or adopt impedance/admittance frameworks for dynamic interaction rather than static compliance.

TABLE III
COMPARISON OF COMPLIANCE ESTIMATION METHODS

References	Stiffness Tunability	Modeling Method	Estimation Error
[30]	P(Yes)	–	–
[28]	TP(Yes)	–	–
[31]	P(Yes)	Potential energy	Only qualitative
[7]	TP(Yes)	Learning model	Only qualitative
[16]	T(No)	Jacobian analysis	Not evaluated
[26]	P(No)	Cosserat	10.0%
Ours	TP(Yes)	ANCF	5.00%

Note: P, Pneumatics; TP, Tendons+Pneumatics; T, Tendons.

V. VALIDATION EXPERIMENTS

To validate the proposed model and control framework, four experiments are conducted on the soft actuator prototype. The kinetostatic model is first validated through feedforward tracking tests with and without external loads. The effect of tendon-length constraints on structural stiffness is then investigated. Finally, the proposed LACC is evaluated under external disturbances for positioning accuracy and load prediction.

A. Hardware Description

Fig. 6 shows the actuator hardware. Maxon EC motors (No. 761267) and 1002 miniature ball screws actuate 1.5 mm 304 stainless-steel wire ropes, with tensions measured by DAYSENSOR miniature high-accuracy force sensors (DYMH-106, 0–30 N). The pneumatic system uses a 160 kPa air pump, X-Valve miniature valves (912-000001-010), and micro pressure sensors (MCP-H10). Control and data acquisition are implemented in MATLAB on a workstation with an Intel i7-12700K CPU (central processing unit) and 32 GB RAM (random access memory). The ANCF-based model and LACC framework are length-agnostic. The element number n can be adjusted for different actuator lengths without modifying the governing equations or control algorithm. A brief convergence check [1] shows that the error decreases from 6.1 to 0.3 mm when the element number n increased from 1 to 6, whereas further refinement significantly increases the computation time (2.95 s at $n = 6$ and 10.74 s at $n = 8$) with diminishing accuracy gains. Therefore, $n = 6$ is used in this study.

B. Open-Loop Position Tracking Experiments

Open-loop trajectory-tracking experiments are conducted to evaluate the shape-estimation accuracy of the kinetostatic model. By solving the IK problem defined in (2), the actuator is commanded to trace three geometries: a 30-mm diameter circle, a 50-mm-diameter spatial dome rose curve, and the letters “SJTU” (Shanghai Jiao Tong University) at $p = 0$ kPa. As shown in Fig. 7, the position root mean square errors (RMSEs), normalized by the original actuator length, remain below 2.5% for all tested trajectories. The largest deviations occur near the trajectory apexes, such as the top of the circle and the letter “S”. This is mainly caused by gravity: the actuator self-weight slightly shifts the upper tendon from the assumed generatrix, causing the model to underestimate the tendon-induced generalized force. The quantitative comparison of open-loop motion

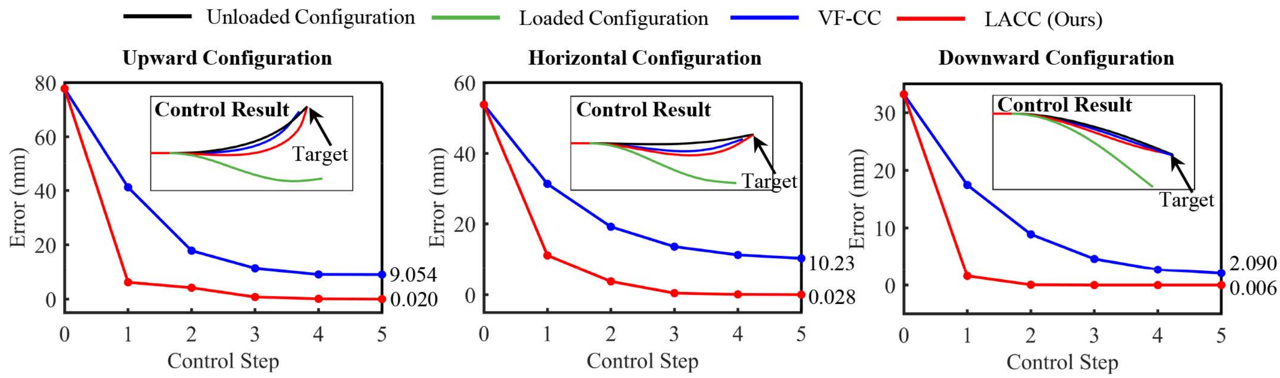

Fig. 5. Control errors of VF-CC [26] and LACC (ours) in (left) upward, (middle) horizontal, and (right) downward configurations. The residual errors after five iterations for each configuration are summarized in Table I.

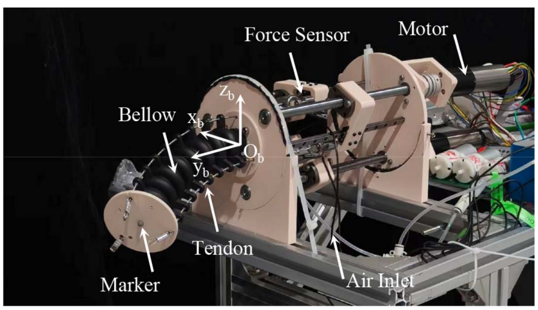

Fig. 6. Experimental setup. The reference coordinate system for the actuator is O_b-$x_by_bz_b$.

control between our model and alternative modeling methods is presented in Table II.

To further evaluate the robustness of the proposed model under external loads, feedforward control experiments with discrete loading are performed under multiple configurations. As illustrated in Fig. 8, a lightweight container (15 g) is suspended from the actuator tip to serve as the baseline payload. Subsequently, the tip load is increased incrementally by adding water in increments of 25, 25, and 50 g. For each loading increment, the required tendon tensions are recalculated by solving the IK problem (2) to maintain the prescribed tip position. Fig. 7 illustrates the actuator's response in two different configurations, with an average steady-state positioning error remaining below 1 mm. The experimental results demonstrate that the proposed model effectively predicts the actuator's configuration with external loads.

C. Stiffness Prediction and Constraint-Induced Enhancement

To demonstrate the stiffness enhancement induced by the fixed-tendon-length constraint when the motors are locked, a series of experiments is conducted. The actuator is first regulated at internal pressures of 0, 25, and 50 kPa. For each pressure, the tension T_1 of the top tendon ($d_1 = 27.5$ mm, $\theta_1 = 0$ rad) is set to $\{0, 1, 2, 3, 4, 5\}$ N, while the other two tendons are kept at 0 N. After the target tension is reached, the motors are locked at zero velocity to impose the fixed-tendon-length constraint. A 50 g payload is then attached to the tip, and the resulting vertical displacement along the z-axis is measured. The equivalent stiffness is calculated as $k_{\text{equivalent}} = (0.05 \times 9.81/z_{\text{unload}} - z_{\text{load}})$ N/m. For each pressure-tension combination, five trials are performed. The results are compared with the theoretical predictions in Fig. 9. Under the fixed-tendon-length constraint, the actuator stiffness is about twice that under the constant-tension condition. The experimental results also agree well with the prediction under the fixed-tendon-length constraint. These results validate the proposed compliance model. Mean errors of the measured stiffness relative to the predicted stiffness are 3.1% (0 kPa), 5.0% (25 kPa) and 3.0% (50 kPa), while maximum relative errors are 4.4% (0 kPa), 5.5% (25 kPa) and 6.0% (50 kPa). The discrepancy arises from three factors: 1) tendon friction, which reduces the effective tension and is neglected in the model; 2) bellows self-contact under large bending, which introduces unmodeled local stiffening; and 3) tendon-length modeling errors caused by gravity-induced deviation from the assumed generatrix, together with experimental measurement uncertainty. Notably, since the LACC framework treats any deviation between the model prediction and the measured response as an apparent tip load and compensates for it iteratively, these unmodeled effects are naturally absorbed into the estimated load term and do not compromise positioning accuracy, as demonstrated by the compliance control experiments in Section V-D.

Table III further highlights the contribution of this work to compliance modeling and control for continuum robots. Most existing robots with extra stiffening structures use the stiffening mechanism itself, but do not quantitatively characterize the resulting compliance variation. Even when compliance is analyzed, the results are usually qualitative and are rarely used for compliance-based control. By contrast, the few studies with quantitative compliance analysis usually focus on simpler robots without extra stiffening structures. The proposed method fills this gap. It enables quantitative compliance modeling for a stiffening-enabled continuum robot and uses the modeled compliance for controller design.

D. Application of Load-Aware Compliance Controller

To evaluate the performance of the proposed load-aware compliance controller (LACC) on the physical actuator, a series

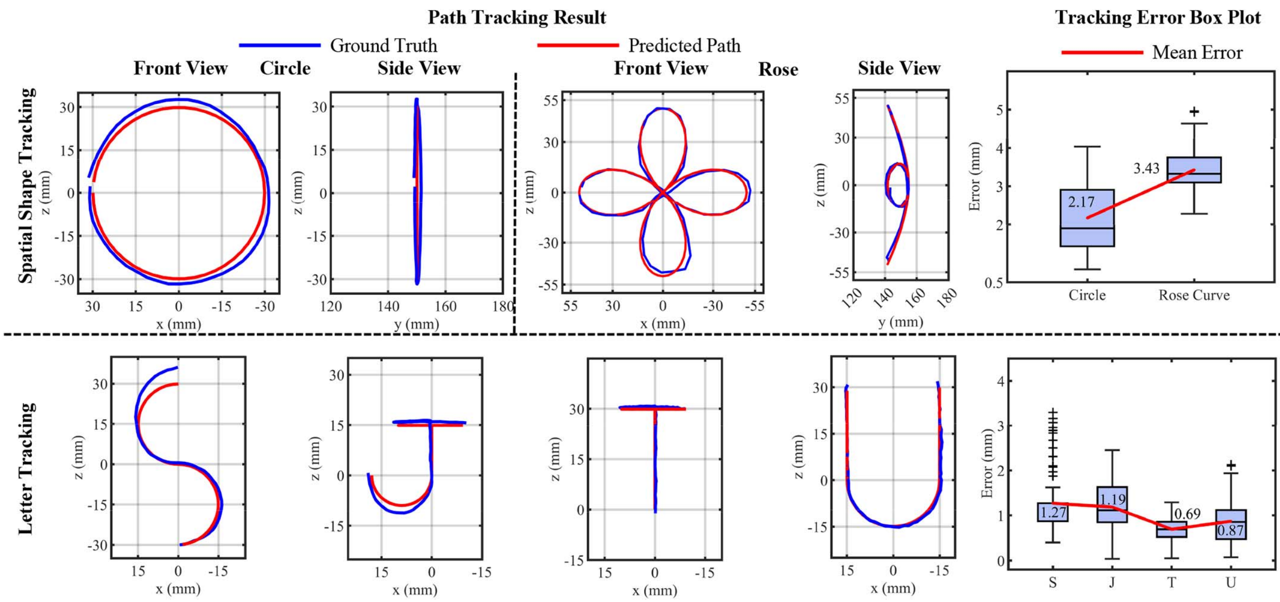

Fig. 7. (Left) path tracking results and (right) tracking error box plot of feedforward control without loads. The actuator is required to track (top) a circle, a 50-mm diameter spatial rose curve and (bottom) "SJTU" letters. The peak deviations primarily occur at the trajectory apexes (e.g., the top of the circle and the letter "S").

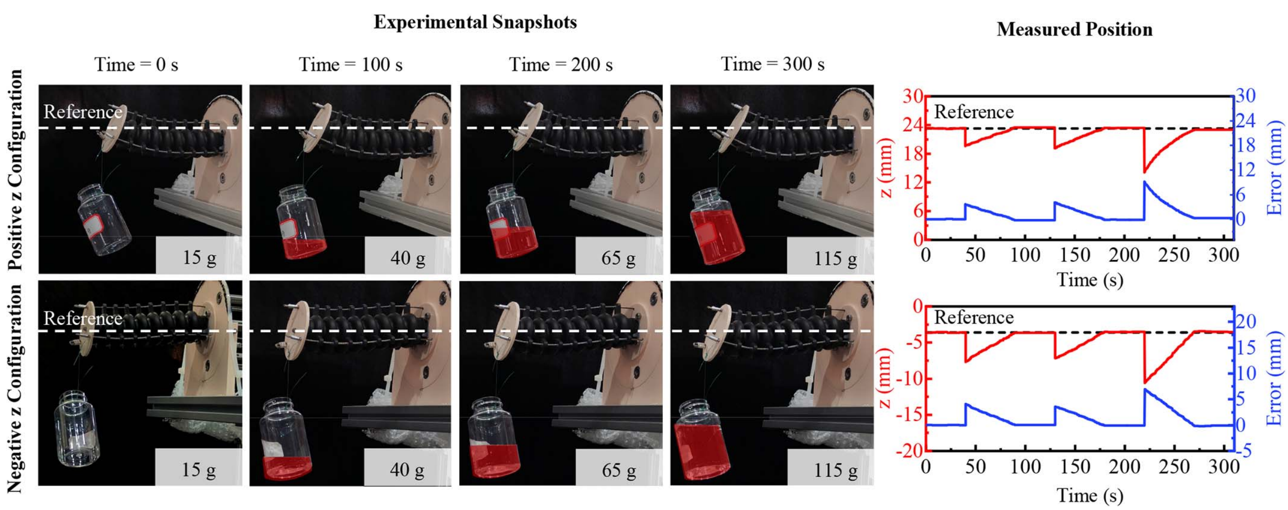

Fig. 8. (Left) experimental snapshots and (right) measured positions of feedforward control with loads. Experiments are conducted in (top) positive z configuration and (bottom) negative z configuration. The water level is indicated by the red shaded area.

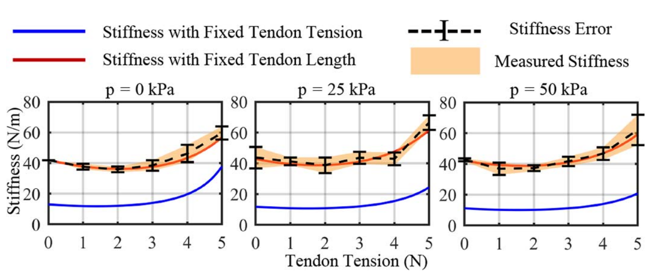

Fig. 9. Measured (black, with error bars) and predicted (red) equivalent stiffness $k_{\text{equivalent}}$ (N/m) versus tendon tension T_1 (N). (left) $p = 0$ kPa, (Middle) $p = 25$ kPa, (right) $p = 50$ kPa.

of loading experiments is conducted. Initially, a 15-g container is suspended from the actuator tip. The actuator is then driven to three representative configurations: upward-bending, horizontal, and downward-bending. Subsequently, water is randomly added to or drained from the container to simulate unpredictable external disturbances. The actuator is required to maintain its original tip position under stochastic loading. Without prior knowledge of the load magnitude, the proposed LACC estimates the instantaneous load based on the measured tip displacement and actively adjusts the tendon lengths to restore and maintain the tip at its original position. The experimental results, as illustrated in Fig. 10, show the iterative load estimation and the corresponding tip trajectory during the compliance control process. The actuator effectively reconfigures its configuration to enhance its load ability.

In the upward configuration, the maximum load is overestimated. The predicted load reaches approximately 100 g despite only 60 g of added water, with overshoot in stages D_3 and D_4. This discrepancy stems from model mismatch under

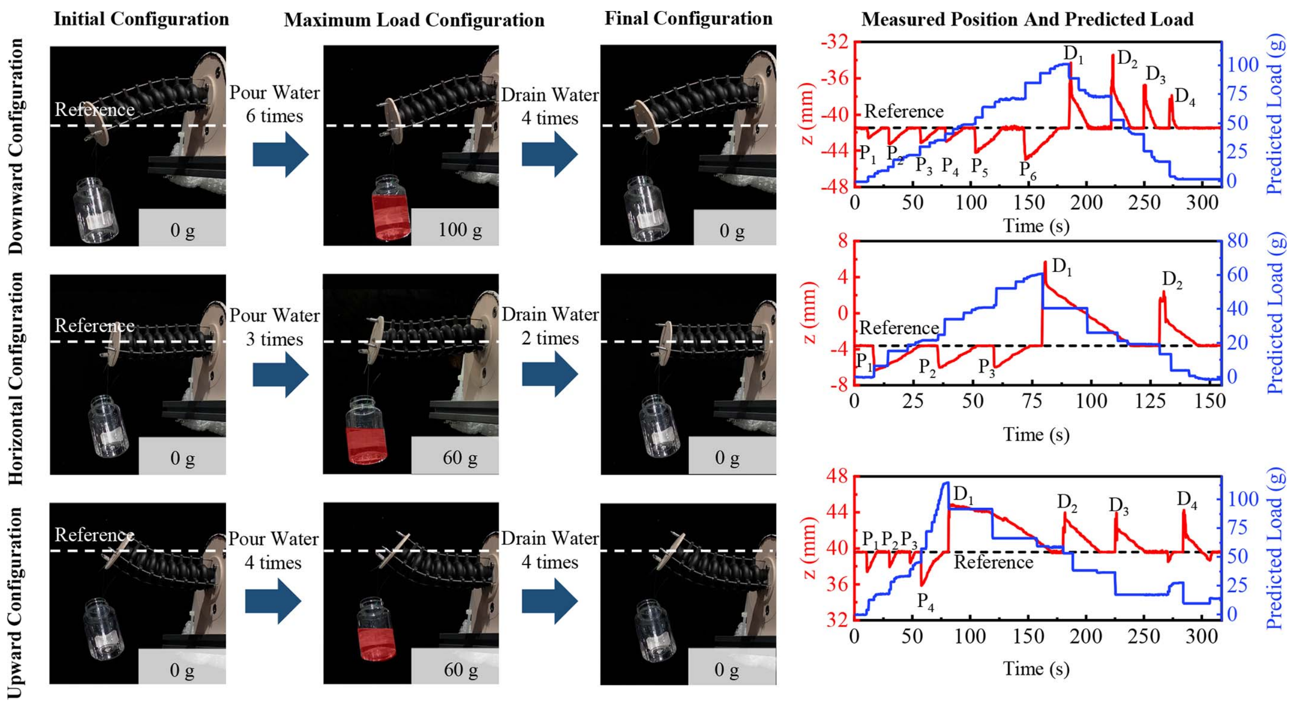

Fig. 10. Compliance control experiments in (top) downward, (middle) horizontal, and (bottom) upward configurations. The actuator undergoes random loading cycles from (left) initial to (middle) maximum load, then unloading cycles to (right) final configuration. Measured positions and predicted loads are shown on the far right. P_i: i-th water pouring; D_i: i-th water draining. Red shaded area: water level.

external load and self-weight. The tendon deviates from the assumed cylindrical generatrix, and inter-hole friction increases. In addition, the ANCF model does not account for bellows self-contact. Under upward bending with applied loads, adjacent bellows convolutions come into contact. This unmodeled behavior further contributes to the error. Nevertheless, LACC maintains the tip position close to its original value, demonstrating effective adaptive interaction despite modeling errors. These errors can be systematically reduced through three model refinements. First, incorporating tendon friction into the generalized tendon force $\mathbf{Q}_c^i$ via a Coulomb model identified from pull-through tests. Second, adding a penalty-based self-contact force term to the equilibrium equations to suppress unmodeled local stiffening. And finally, replacing the constant tendon routing radius d_i with a bending- and tension-dependent value to correct the gravity-induced tendon-path deviation.

E. Continuous and Cyclic Loading Validation

To evaluate the LACC under time-varying loads rather than the discrete step-loading protocol in Section V-D, a continuous loading experiment is conducted. The experimental setup is the same as in Fig. 10. Water is gradually added to and subsequently drained from the tip container, producing a continuously varying external load over a 50-s period. The actuator is regulated in the horizontal configuration, and the LACC is activated throughout the experiment.

As shown in Fig. 11(a), the predicted load increases continuously from 0 g to approximately 110 g during the loading phase (0–35 s), then decreases during the unloading phase (35–50 s). Without the LACC, the tip drifts downward by over 10mm under the increasing load (black curve). With the LACC active, the tip position (blue curve) remains within 0.722 mm of the reference throughout the entire loading and unloading process, demonstrating that the iterative load estimation and compliance-based compensation remain effective under continuously varying loads. In contrast, the cyclic loading experiment [Fig. 11(b)] reveals a clear limitation: under repeated loading-unloading cycles, the LACC maintains the tip position within 3.573 mm, substantially worse than the 0.722 mm achieved under slow-varying loads. This degraded performance arises because the iterative load observer cannot complete convergence before the load direction reverses in each cycle. The LACC is effective when the rate of load variation is slow relative to the controller's convergence time (approximate 0.5 s, including IK solving and motor command execution). However, it is important to acknowledge the framework's boundary. Under impulsive load changes, the controller requires several iterations to re-estimate the load and re-converge, during which a transient positioning error occurs. Under high-frequency cyclic loading (e.g., above 0.125 Hz), the iterative scheme cannot complete convergence within each cycle, leading to accumulating tracking errors. These limitations arise from two factors: 1) the computational latency of the ANCF-based IK solver; and 2) the finite response speed of the tendon-drive motors. Fundamentally, the quasi-static equilibrium assumption underlying the compliance formulation is violated when inertial

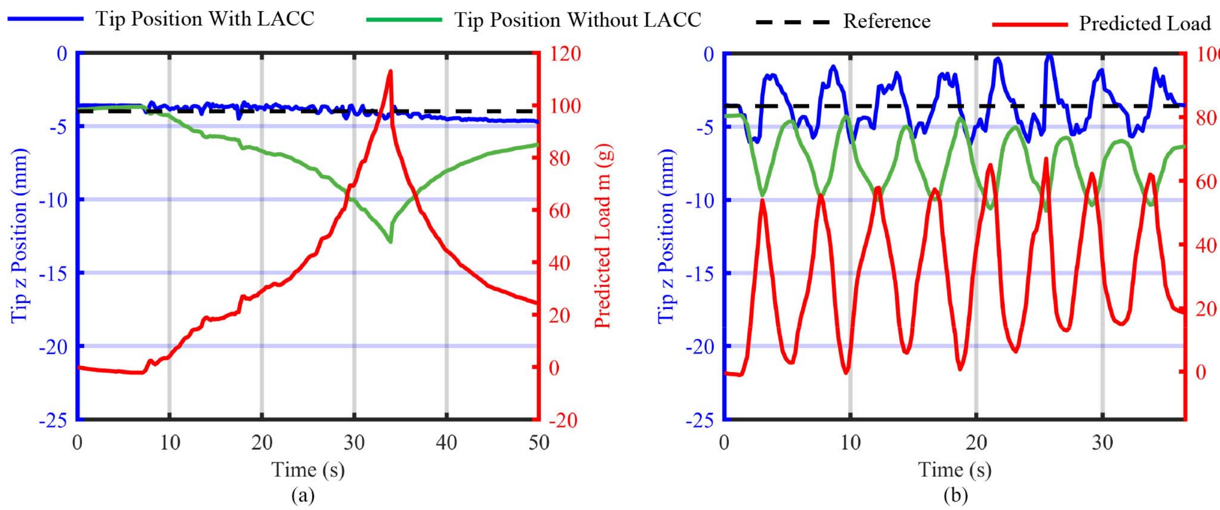

Fig. 11. (a) Continuous loading experiment in the horizontal configuration. Water is gradually added to and then drained from the tip container, producing a continuously varying load. The LACC maintains the tip position (blue) within 0.722 mm of the reference (black), while the uncontrolled tip (black) drifts by over 10 mm. (b) Cyclic loading experiment. Water is added to and then drained from the tip container, producing a cyclic load of 0.125 Hz. The LACC maintains the tip position within 3.573 mm of the reference, while the uncontrolled tip drifts by over 7 mm.

and damping effects become nonnegligible under rapid load dynamics. Extending the framework to such dynamic scenarios requires incorporating the ANCF-based inertia matrix and experimentally identified damping into a dynamic formulation, which is identified as a key direction for future work.

VI. Conclusion

This article presents a compliance modeling and control framework for TPHD bellows-shaped soft actuators. It derives analytical compliance formulations under both constant-tendon-force and fixed-tendon-length constraints to regulate the actuator tip position and stiffness. Simulation and experimental results validate the proposed method. The LACC achieves a tip positioning error below 0.03 mm within five control iterations. Under simulated stochastic loading, LACC reduces the tip positioning error by over 99.7% compared with the conventional virtual-force-based compliance controller [25]. Experimentally, the proposed compliance model achieves an average compliance-estimation error of 5.0%, representing a 50% reduction relative to the 10.0% error of prior Cosserat-based approaches [25]. Experiments in real-world tasks also demonstrate improved payload capacity and environmental adaptability of the bellows-shaped soft actuator. Although the current framework is limited to predicting the tip load of the actuator, it provides a promising foundation for future extension to distributed load estimation and more general interaction-aware compliance control of soft actuators.

Two limitations of the present framework warrant explicit discussion. First, the kinetostatic model and LACC are derived under a static equilibrium assumption, making them suitable for quasi-static tasks where inertial and damping effects are negligible. Under fast dynamic maneuvers or impact-like disturbances, unmodeled inertial coupling and viscoelastic damping would introduce additional positioning errors. Incorporating the ANCF-based inertia matrix and experimentally identified damping into the compliance formulation is identified as a key direction for extending the framework to dynamic scenarios. Second, the current single-segment configuration limits the dexterity required for highly unstructured environments. Multi-segment extension would involve concatenating ANCF segments with inter-segment constraints, enabling spatial obstacle avoidance and on-demand stiffness distribution along the actuator body. Future work will address both directions to broaden the applicability of the proposed framework.

Regarding the tendon-pneumatic hybrid system's hardware complexity, it is important to note that the additional actuators and sensors are justified by the unique capability of simultaneous position and stiffness regulation. Compared with antagonistic dual-chamber pneumatic actuators that require redundant chambers for multi-DOF motion, the tendon-pneumatic design achieves a more compact form factor while providing explicit modelability for analytical compliance characterization. The modest increase in hardware cost is offset by the enhanced functionality, including continuous stiffness regulation, high force output, and the ability to implement the proposed LACC framework.

From a practical deployment perspective, several directions warrant discussion. Untethered operation would require miniaturized pneumatic supplies, embedded motor drivers, and wireless communication, which are primarily integration engineering challenges. The proposed compliance modeling and control framework would remain directly applicable once such a platform is realized. Miniaturization to surgical scales (e.g., 10 mm diameter) introduces proportionally larger tendon friction that would require the inclusion of friction in the model. Integration with surgical tools or robotic grippers adds tip payloads, which the LACC can naturally absorb into the estimated load term $\hat{\mathbf{F}}_e$, provided the end-effector is rigidly attached. These practical directions are identified as important avenues for translating the present framework to field-deployable applications.

References

[1] Y. Rong and G. Gu, "Kinetostatic modeling and position-orientation control of bellow-shaped soft continuum robots," *IEEE/ASME Trans. Mechatron.*, vol. 31, no. 3, pp. 3745–3756, Jun. 2026.

[2] Z. Song, C. Wei, Z. Wang, B. Liu, X. Zhang, and Y. Song, "A reconfigurable soft actuator with tunable deformation and stiffness," *Adv. Mater. Technol.*, vol. 10, no. 19, 2025, Art. no. e00772.

[3] R. Toyoda et al., "A stretchable jamming gripper grasping flat plates," *IEEE Access*, vol. 12, pp. 48764–48773, 2024.

[4] J. H. Park et al., "Cooperative antagonistic mechanism driven by bidirectional pneumatic artificial muscles for soft robotic joints," *Mechatronics*, vol. 97, 2024, Art. no. 103099.

[5] J. Xia et al., "Discrete pneumatic-tendon-coupled actuators with interconnected air circuit for untethered soft robots," *Adv. Intell. Syst.*, vol. 7, no. 4, 2025, Art. no. 2400533.

[6] H. Yang et al., "Multi-segment extendable soft manipulator driven by a pneumatic-tendon coupling mechanism," *Biomimetics*, vol. 10, no. 10, pp. 1–16, 2025, Art. no. 643.

[7] X. Fu et al., "Adaptive kinematic and stiffness control of a hybrid-driven soft robot for enhanced interactions under external loads," *Results Eng.*, vol. 28, 2025, Art. no. 107955.

[8] A. Öchsner, *Euler–Bernoulli Beam Theory.* Cham, Switzerland: Springer Int. Publishing, 2021, pp. 7–66.

[9] A. Stilli, E. Kolokotronis, J. Fraś, A. Ataka, K. Althoefer, and H. A. Wurdemann, "Static kinematics for an antagonistically actuated robot based on a beam-mechanics-based model," in *Proc. IROS*, 2018, pp. 6959–6964.

[10] R. J. WebsterIII and B. A. Jones, "Design and kinematic modeling of constant curvature continuum robots: A review," *Int. J. Robot. Res.*, vol. 29, no. 13, pp. 1661–1683, 2010.

[11] D. Drotman, M. Ishida, S. Jadhav, and M. T. Tolley, "Application-driven design of soft, 3-D printed, pneumatic actuators with bellows," *IEEE/ASME Trans. Mechatron.*, vol. 24, no. 1, pp. 78–87, Feb. 2019.

[12] S. Lin, Y. Wang, A. Li, and W. Chen, "The piecewise constant curvature model for the forward and inverse kinematics of continuum robot based on lie theory," in *Proc. ICARM*, 2023, pp. 386–391.

[13] H. Wang, J. Du, and Y. Mao, "Cosserat rod-based tendon friction modeling, simulation, and experiments for tendon-driven continuum robots," *Micromachines*, vol. 16, no. 3, 2025, Art. no. 346.

[14] J. Shi, S.-A. Abad, J. S. Dai, and H. A. Wurdemann, "Position and orientation control for hyperelastic multisegment continuum robots," *IEEE/ASME Trans. Mechatron.*, vol. 29, no. 2, pp. 995–1006, Apr. 2024.

[15] C. B. Black, J. Till, and D. C. Rucker, "Parallel continuum robots: Modeling, analysis, and actuation-based force sensing," *IEEE Trans. Robot.*, vol. 34, no. 1, pp. 29–47, Feb. 2018.

[16] S. Lilge and J. Burgner-Kahrs, "Kinetostatic modeling of tendon-driven parallel continuum robots," *IEEE Trans. Robot.*, vol. 39, no. 2, pp. 1563–1579, Apr. 2023.

[17] J. Shi, A. Shariati, S.-A. Abad, Y. Liu, J. S. Dai, and H. A. Wurdemann, "Stiffness modelling and analysis of soft fluidic-driven robots using lie theory," *Int. J. Robot. Res.*, vol. 43, no. 3, pp. 354–384, 2024.

[18] M. Bensch, T.-D. Job, T.-L. Habich, T. Seel, and M. Schappler, "Physics-informed neural networks for continuum robots: Towards fast approximation of static cosserat rod theory," in *Proc. ICRA*, 2024, pp. 17293–17299.

[19] J. Liu, Y. Duo, X. Chen, Z. Zuo, Y. Liu, and L. Wen, "Data-driven methods for sensing, modeling and control of soft continuum robot: A review," *IEEE/ASME Trans. Mechatron.*, vol. 30, no. 6, pp. 5520–5530, Dec. 2025.

[20] D. Bruder, C. D. Remy, and R. Vasudevan, "Nonlinear system identification of soft robot dynamics using Koopman operator theory," in *Proc. ICRA*, 2019, pp. 6244–6250.

[21] J. Gerstmayr, H. Sugiyama, and A. Mikkola, "Review on the absolute nodal coordinate formulation for large deformation analysis of multibody systems," *J. Comput. Nonlinear Dyn.*, vol. 8, no. 3, 2013, Art. no. 031016.

[22] A. A. Shabana and R. Y. Yakoub, "Three dimensional absolute nodal coordinate formulation for beam elements: Theory," *J. Mech. Des.*, vol. 123, no. 4, pp. 606–613, 2001.

[23] X. Huang, Z. Yuan, X. Yang, and G. Gu, "Precise control of soft robots amidst uncertain environmental contacts and forces," *IEEE Trans. Robot.*, vol. 40, pp. 3565–3580, 2024.

[24] X. Huang, Y. Rong, and G. Gu, "High-precision dynamic control of soft robots with the physics-learning hybrid modeling approach," *IEEE/ASME Trans. Mechatron.*, vol. 30, no. 3, pp. 1658–1669, Jun. 2025.

[25] J. Shi, S.-A. Abad, G. Shi, W. Gaozhang, J. S. Dai, and H. A. Wurdemann, "Model-based static compliance analysis and control for pneumatic-driven soft robots," *IEEE/ASME Trans. Mechatron.*, vol. 30, no. 6, pp. 5567–5578, Dec. 2025.

[26] K. Oliver-Butler, J. Till, and C. D. Rucker, "Continuum robot stiffness under external loads and prescribed tendon displacements," *IEEE Trans. Robot.*, vol. 35, pp. 403–419, 2019.

[27] X. Li et al., "Disturbance-adaptive tapered soft manipulator with precise motion controller for enhanced task performance," *IEEE Trans. Robot.*, vol. 40, pp. 3581–3601, 2024.

[28] X. Huang, J. Zou, and G. Gu, "Kinematic modeling and control of variable curvature soft continuum robots," *IEEE/ASME Trans. Mechatron.*, vol. 26, no. 6, pp. 3175–3185, Dec. 2021.

[29] L.-J. Gai, J. Huang, and X. Zong, "Stiffness-tunable soft bellows actuators by cross-fiber jamming effect for robust grasping," *IEEE/ASME Trans. Mechatron.*, vol. 28, no. 5, pp. 2897–2907, Oct. 2023.

[30] D. Bruder, M. A. Graule, C. B. Teeple, and R. J. Wood, "Increasing the payload capacity of soft robot arms by localized stiffening," *Sci. Robot.*, vol. 8, no. 81, 2023, Art. no. 9001.

Zhanxuan Peng is currently working toward the Ph.D. degree in mechanical engineering with Shanghai Jiao Tong University, Shanghai, China.

His research interests include modeling and control of soft continuum robots.

Yu Rong received the B.E. degree in mechatronic engineering from the Northwestern Polytechnical University, Xi'an, China, in 2019. He is currently working toward the Ph.D. degree in mechatronic engineering with Shanghai Jiao Tong University, Shanghai, China.

His research interests include modeling and control of soft continuum robots.

Zhenpu Zhu is currently working toward the Ph.D. degree in mechanical engineering with Shanghai Jiao Tong University, Shanghai, China.

His research interests include modeling and control of hyper-redundant manipulators.

Jieji Ren received the B.Sc. and M.Sc. degrees in optics from Harbin Institute of Technology, Harbin, China, in 2013 and 2015, respectively, and the Ph.D. degree in mechatronic engineering from Shanghai Jiao Tong University, Shanghai, China, in 2022.

Since 2022, he has been with Shanghai Jiao Tong University as an Assistant Researcher. His research interests include camera-based tactile sensing and its applications in soft robotics.

Guoying Gu (Senior Member, IEEE) received the B.E. degree (Hons.) in electronic science and technology and the Ph.D. degree (Hons.) in mechatronic engineering from Shanghai Jiao Tong University, Shanghai, China, in 2006 and 2012, respectively.

He was a Humboldt Fellow with the University of Oldenburg, Oldenburg, Germany. He was a Visiting Scholar with Massachusetts Institute of Technology, Cambridge, MA, USA; the National University of Singapore, Singapore; and Concordia University, Montreal, QC, Canada. He is currently a Distinguished Professor with the School of Mechanical Engineering, Shanghai Jiao Tong University. He has authored or co-authored over 150 publications, including articles in *Science*, *Science Robotics*, *Nature Biomedical Engineering*, *Nature Reviews Materials*, *Nature Materials*, *Nature Communications*, *Science Advances*, *Advanced Materials*, *Soft Robotics*, Science China series, IEEE/ASME TRANSACTIONS journals, book chapters, and international conference proceedings. His research interests include soft robotics, bioinspired and wearable robots, and smart materials for sensing, actuation, and motion control.

Dr. Gu was a recipient of the National Science Fund for Distinguished Young Scholars and the XPLORER Prize. He is currently an Associate Editor for *Soft Robotics, Soft Science,* and IEEE TRANSACTIONS ON AUTOMATION SCIENCE AND ENGINEERING, and previously served as an Associate Editor for IEEE TRANSACTIONS ON ROBOTICS and IEEE ROBOTICS AND AUTOMATION LETTERS.